nature catalysis

ARTICLES

https://doi.org/10.1038/s41929-019-0380-x

Constraining CO coverage on copper promotes high-efficiency ethylene electroproduction

Jun Li[1,2,5], Ziyun Wang[2,5], Christopher McCallum[1,5], Yi Xu[1], Fengwang Li[2], Yuhang Wang[2], Christine M. Gabardo[1], Cao-Thang Dinh[2], Tao-Tao Zhuang[2], Liang Wang[3], Jane Y. Howe[4], Yang Ren[3], Edward H. Sargent[2*] and David Sinton[1*]

The availability of inexpensive industrial CO gas streams motivates efficient electrocatalytic upgrading of CO to higher-value feedstocks such as ethylene. However, the electrosynthesis of ethylene by the CO reduction reaction (CORR) has suffered from low selectivity and energy efficiency. Here we find that the recent strategy of increasing performance through use of highly alkaline electrolyte—which is very effective in CO_2RR—fails in CORR and drives the reaction to acetate. We then observe that ethylene selectivity increases when we constrain (decrease) CO availability. Using density functional theory, we show how CO coverage on copper influences the reaction pathways of ethylene versus oxygenate: lower CO coverage stabilizes the ethylene-relevant intermediates whereas higher CO coverage favours oxygenate formation. We then control local CO availability experimentally by tuning the CO concentration and reaction rate; we achieve ethylene Faradaic efficiencies of 72% and a partial current density of >800 mA cm^{-2}. The overall system provides a half-cell energy efficiency of 44% for ethylene production.

The electrochemical upgrading of CO_2 into carbon-based chemicals and fuels provides a means to close the anthropogenic carbon cycle and store excess renewable electricity[1–3]. Much effort has been dedicated to the production of valuable two-carbon (C_2) products by direct CO_2 electrolysis[4–7]. Ethylene is an electrolysis product of particular interest due to the high demand for it as a chemical feedstock.

Starting with CO instead of CO_2 as a feedstock avoids carbonate formation in alkaline CO_2 electrolysers and thus overcomes issues in feedstock utilization and stability[8,9]. Furthermore, CO gas feedstock streams are available industrially at a range of purities. Abundant and inexpensive manufactured gases such as syngas, coal gas and producer gas—and also effluent streams from steel manufacturing—have CO concentrations in the range of 10–60% (ref. [10–14]). Gas purification of these streams is costly, as indicated by the sale price of high purity CO, which is over ten times that of commercial CO streams with low purities (for example, syngas)[15]. These costs will be avoided once available dilute CO gas streams—whether they are manufactured or effluent—are upgraded to ethylene with high efficiency.

Recent advances in the CO reduction reaction (CORR) for ethylene production have focused on increasing the reaction rate and selectivity[8,9,16–19]. At moderate current densities (~100 mA cm^{-2}), CO to ethylene has been demonstrated on nanostructured copper catalysts employing gas diffusion electrodes that overcome mass transfer limitations[9,16–18]. Increasing the alkalinity of the electrolyte has increased the activity and selectivity for ethylene in both the CO_2RR (ref. [4]) and CORR (ref. [9]); however, even with concentrated KOH electrolytes and pure CO reactant gas, the highest reported CO to ethylene Faradaic efficiency (FE) remains ~40% with a cathodic energy efficiency of ~20% (ref. [9]).

Here we present high-efficiency ethylene electroproduction from CO on copper at current densities above 100 mA cm^{-2}. The system performs well across a wide range of input CO concentrations. We find that there is increased ethylene selectivity when we reduce CO availability to the CO mass transport limit by operating at high current densities. This finding motivates us to investigate the link between local CO availability and ethylene selectivity. Using density functional theory (DFT) calculations, we first assess—as a function of CO coverage—the activation energies and enthalpy changes of the key elementary steps that branch the ethylene versus oxygenate pathways. We find that lowering CO coverage on copper benefits the ethylene pathway both thermodynamically and kinetically. In experiments, we constrain the local CO concentration at the catalyst–electrolyte interface by tuning the combination of the CO supply concentration and reaction rate (for example, applying high reaction rates for high input CO concentrations). We achieve an ethylene partial current density >800 mA cm^{-2} and a $FE_{ethylene}$ of over 70% across a wide range of CO concentrations (5–100%) by implementing this strategy. By combining high selectivity with low overpotential, we achieve a 44% half-cell energy efficiency for ethylene production.

Results

The effect of the KOH concentration. Hydroxide ions have—in the context of CO_2 reduction—been shown to play a crucial role in promoting both selectivity and activity in ethylene production. They do so when they bring the onset of ethylene production closer to that of CO (ref. [4]). A subsequent CORR flow-cell study with an increasing KOH concentration from 0.1 M to 1 M further demonstrated increased ethylene production by the suppression of hydrogen generation[9].

To assess the effect of electrolyte alkalinity on ethylene production from the CORR, we varied the KOH concentration from 1 M to 5 M and carried out the CORR in highly alkaline conditions in

[1]Department of Mechanical and Industrial Engineering, University of Toronto, Toronto, Ontario, Canada. [2]Department of Electrical and Computer Engineering, University of Toronto, Toronto, Ontario, Canada. [3]X-ray Science Division, Argonne National Laboratory, Lemont, IL, USA. [4]Hitachi High Technologies America, Clarksburg, MD, USA. [5]These authors contributed equally: Jun Li, Ziyun Wang and Christopher McCallum *e-mail: ted.sargent@utoronto.ca; sinton@mie.utoronto.ca

a flow cell electrolyser (Supplementary Fig. 1)[4–6,20]. Copper oxide precatalysts (see Methods) were deposited and then reduced to active copper catalysts in the CORR.

We found that increasing the alkalinity of the electrolyte above 1 M decreased ethylene electroproduction (Fig. 1a) and increased acetate formation (Supplementary Fig. 2). The increase of $FE_{acetate}$ with elevated KOH concentration can be attributed to the reaction of concentrated hydroxide ions with CORR intermediates that are relevant to ethylene, ethanol and 1-propanol[8,9,21]. In the case of alkaline CO_2 electroreduction, this interaction of hydroxide ions and intermediates is not substantial due to the pH-moderating influence of dissolved CO_2 (ref. [4]); the concentration of hydroxide ions is more than one order of magnitude lower than under the CORR at similar current and bulk electrolyte conditions[9].

Under the electrolyte concentrations tested, $FE_{ethylene}$ increased with applied potential/current (Fig. 1a) and peaked just before a sharp increase in hydrogen production (Supplementary Fig. 3). Specifically, decreasing the potential from −0.2 to −0.6 V versus a reversible hydrogen electrode (RHE) in 5 M KOH resulted in a linear increase of $FE_{ethylene}$ (0.8–58%) and an exponential increase in the ethylene partial current density (0.06–728 mA cm^{-2}) (Fig. 1b). By carrying out a reaction–diffusion model analysis, we found a dramatic decrease in the local CO concentration at the catalyst layer due to increased reaction kinetics and thereby a buildup of hydroxide ions; that is, an increase in local pH. A further increase in overpotential leads to severe depletion in the local CO availability as a result of rapid ethylene formation, a sharp increase of hydrogen binding and evolution (Supplementary Fig. 4), and thereby a reduction of $FE_{ethylene}$. The shift to hydrogen signals the onset of CO mass transport limits and represents the lower limit of CO availability for efficient ethylene production.

We then determined the cathodic energy efficiency for ethylene production from the measured overpotential and ethylene selectivity (Supplementary Fig. 5 and Supplementary Note 1). The highest ethylene cathodic energy efficiency of 35% was achieved when we used 1 M KOH. Improving this energy efficiency further would require increased ethylene selectivity at a lower overpotential. Results here (Fig. 1) indicate that increasing electrolyte alkalinity will not increase ethylene selectivity further; however, reaction-rate driven changes in local CO availability can influence ethylene selectivity. We therefore hypothesized that independently controlling local CO concentration at the catalyst surface could offer a route to advance ethylene production efficiency.

DFT calculations. We sought to understand the connection between the local CO concentration and the ethylene versus oxygenate formation pathways with the aid of DFT. Previous reports correlate the ethylene/oxygenate production from CO reduction with the hydrogenation of oxygen-containing intermediates[22–24], indicating that the intermediate state is likely to proceed towards ethylene once all of the oxygen-containing groups are removed by hydrogenation to form water. Specifically, *CHCOH (denoted IM, Fig. 2a) has been identified as the key intermediate for hydrogenation into ethylene and oxygenates[23]: the hydroxyl group can be deoxidized, forming *CCH (IM-C), which leads to ethylene, whereas hydrogenation of the intermediate into *CHCHOH (IM-O) instead favours the production of oxygenates. We questioned whether controlling the IM reduction step to encourage the C-pathway (IM-C) instead of the O-pathway (IM-O) could promote ethylene production.

We predicted the geometries of IM, IM-C and IM-O on Cu(100) using DFT calculations (Fig. 2a). We note that the main difference between the IM-O and IM-C states is the degree of unsaturation (Supplementary Note 2), namely 2.5 for IM-C and 1.5 for IM-O; IM-C thus requires greater surface bonding ability to be stabilized. As the adsorption of intermediates is affected by the surface coverage of CO due to adsorbate–adsorbate interactions[25], tuning the surface bonding ability of IM-C by controlling the coverage of adsorbed *CO could influence the relative stability of ethylene-forming IM-C versus IM-O.

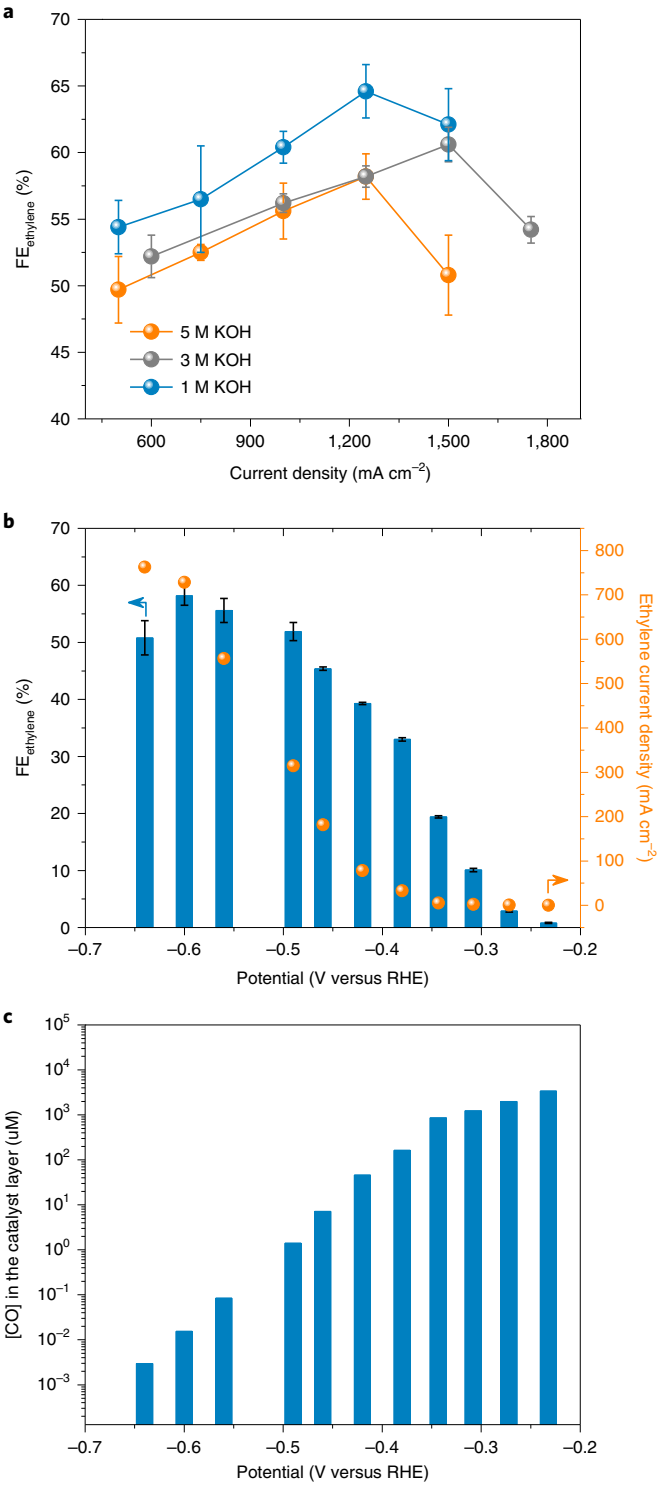

Fig. 1 | The influence of the KOH concentration on CO reduction. a, A comparison of $FE_{ethylene}$ at various KOH concentrations as a function of the applied current density. **b**, The $FE_{ethylene}$ and partial current density from CO reduction in 5 M KOH as a function of the applied potential. **c**, The simulated local CO concentration in the catalyst layer as a function of applied potential in 5 M KOH. Error bars are means ± s.d. ($n = 3$ replicates).

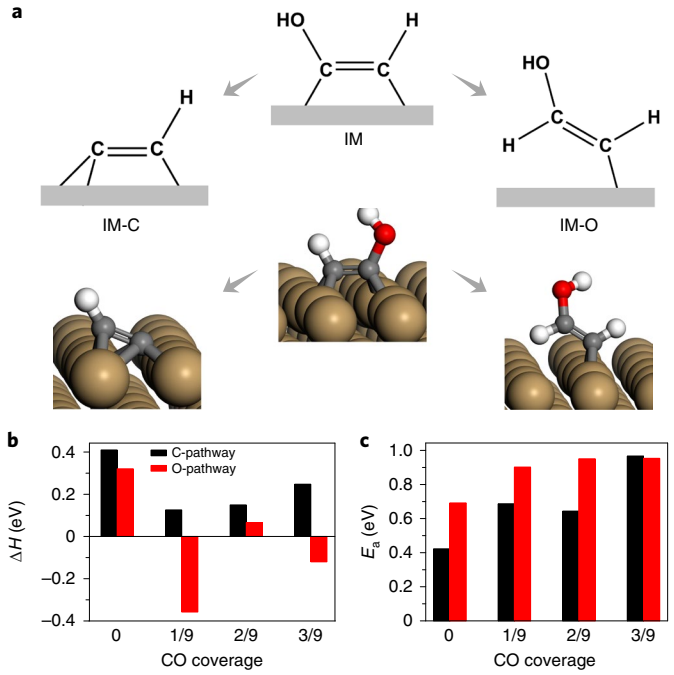

Fig. 2 | DFT calculation results on effects of *CO coverage. a, A schematic plot of the reaction mechanism where the last oxygen-containing group in *CHCOH (IM) is removed, forming *CCH (IM-C), and an alternative pathway to *CHCHOH (IM-O), as well as the geometries of IM, IM-C and IM-O on Cu(100) surfaces. Yellow, copper; grey, carbon; red, oxygen; white, hydrogen. **b**, The enthalpy changes for the C- and O-pathways at different levels of CO coverage. **c**, The relation between coverage and activation energy (E_a) for these two pathways.

We first calculated the reaction energies of the C- and O- pathways (Fig. 2b); the reaction energies are similar at zero CO coverage, and the O-pathway becomes more favourable at higher CO coverages. Noting the key role of kinetics in these reactions[22], we used an explicit water model to calculate the energies of the three intermediate states (IM, IM-C, IM-O) and the associated transition states (TS-C and TS-O), with the *CO coverage ranging from 0 to 3/9 (Supplementary Figs. 6–15)[26]. A coverage of 3/9 was selected on the basis of a kinetic modelling prediction of ~0.3 ML CO coverage on copper surfaces[27]. We found that the barriers to both the C- and O- pathways grow with increasing CO coverage (Fig. 2c). At low CO coverage the C-pathway is kinetically favoured over the O-pathway whereas the O-pathway becomes more favourable at 3/9 ML. These models do not indicate the species expected: acetate, ethanol and 1-propanol; however, both the reaction energy and enthalpy calculations indicate that an oxygenate-forming O-pathway is favoured at higher CO coverages.

We also calculated the effects of CO coverage on the CO dimerization barriers and enthalpy changes (Supplementary Figs. 16–22). Both show decreased values as CO coverage increases, indicating that high CO coverage favours CO dimerization. The barrier to CO dimerization at 2/9 ML (with two CO reactants and no other adsorbed CO) is calculated to be 0.66 eV, which is lower than the threshold (0.75 eV) for fast kinetics[28], suggesting that dimerization is not limiting under these conditions. We further assessed the barriers of the C- and O- pathways with applied potentials (Supplementary Fig. 23)[27,29]. These barriers are lower than those associated with CO dimerization at similar CO coverages, which suggests that CO dimerization is the rate-determing step, consistent with previous findings[28,30].

These DFT simulations predict that limiting the surface coverage of CO would favour ethylene production. In practice, CO coverage can be limited by increasing the reaction rate, but not without higher overpotentials and reduced efficiency. An independent means of controlling CO coverage is by the local CO concentration or CO partial pressure (p_{CO}), where the local CO concentration correlates with p_{CO} by Henry's law. At equilibrium, the surface coverage of CO (θ_{CO}) is directly proportional to the local CO partial pressure, as given by equation[31,32]:

$$\theta_{CO} = \theta_* p_{CO} e^{-\frac{E_{CO}}{RT}} \quad (1)$$

where θ_* is the coverage of free surface sites, E_{CO} is the CO adsorption energy on the surface, R is the ideal gas constant and T is the temperature. To achieve low coverage of CO favoring ethylene production, decreasing the partial pressure of CO at catalysts layer is therefore a promising approach.

Materials characterization. To explore the implications of the DFT results experimentally, we pursued CORR across a wide range of CO supply gas concentrations by dilution with N_2, beginning with in situ catalyst derivation (Fig. 3a). Copper catalysts that are derived from oxide precatalysts (Supplementary Fig. 24) at CO concentrations of 100% (Fig. 3b) and 2.5% (Fig. 3c) both show a similar morphology of aggregated nanoparticle structures. Operando X-ray absorption spectra at the copper K-edge exhibit pure metallic copper features from the catalysts derived at all of the tested CO concentrations (Fig. 3d and Supplementary Fig. 25). High-resolution operando X-ray diffraction analysis[33] further confirms that a stable metallic copper structure remains the active catalyst during the CORR operation under these conditions (Fig. 3e and Supplementary Fig. 26).

The influence of the CO gas concentration. We evaluated the performance of the CORR as a function of the input CO gas concentration in 1 M KOH across a range of applied potentials. When we varied the incoming CO concentration from 2.5 to 100% (in an inert N_2 carrier gas), we observed an overall increase of both the total current density (Supplementary Fig. 27) and the CORR partial current density (Fig. 4a,b). The enhancement of the current density follows an exponential increase in the potential window of −0.32 V to −0.52 V versus RHE at CO concentrations of 2.5%, 5% and 10%. The exponential trend extends further to potentials of −0.66 V and −0.72 V versus RHE at the highest CO concentrations of 50% and 100%, respectively. These trends indicate abundant mass transport (no mass transport limitation) over these potential ranges[9]. At a higher overpotential, the current density trend is curbed due to CO mass transport limitation (Fig. 4a,b and Supplementary Fig. 27)[8], with a characteristic increase in hydrogen production (Supplementary Fig. 28).

$FE_{ethylene}$ increases with applied potential to a peak value that corresponds to the onset of mass transport limitation that is observed in the current output (Fig. 4c,d). The results show similar ethylene partial current densities when operating at different CO concentrations without CO mass transport limitation (Supplementary Fig. 29), in agreement with a previous report[34]. With 2.5% CO, a peak FE of 51% is reached, which is commensurate with a 32% FE of hydrogen at −0.53 versus RHE (Supplementary Fig. 28). For cases in which the CORR performed at 5% and 10% CO conditions, we achieve 72% $FE_{ethylene}$ at −0.52 V versus RHE with a considerable decrease in hydrogen production (Supplementary Fig. 28). Further increasing the CO concentration to 50% and 100% results in peak ethylene production of ~70% at higher potentials of −0.66 V and −0.72 V versus RHE, with ethylene partial current densities of 509 mA cm^{-2} and 808 mA cm^{-2}, respectively. By levering the dependence of the overpotential and ethylene selectivity on the input CO concentration, we achieved 44% cathodic energy efficiency for ethylene production using 5% CO (Supplementary Note 1).

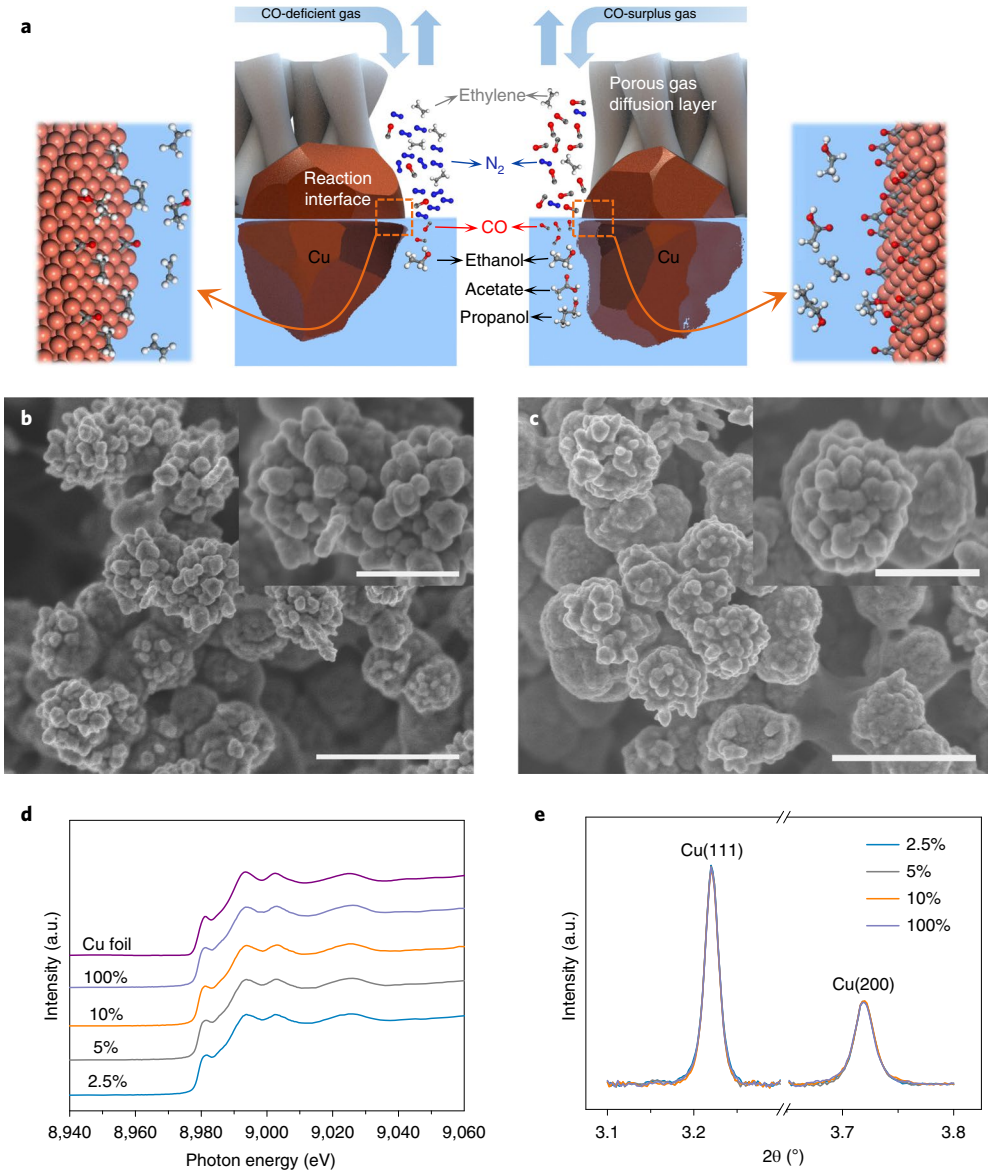

Fig. 3 | Characterization of the copper electrocatalysts. a, A schematic illustration of porous gas diffusion electrodes with CO reduction at the catalyst–electrolyte interface, showing how the CO-deficiency and CO-surplus conditions influence product selectivity. **b**,**c**, SEM images of derived copper catalysts at CO concentrations of 100% (**b**) and 2.5% (**c**); the scale bars are both 500 nm. The insets are the respective high-resolution SEM results with scale bars of 200 nm. **d**,**e**, Operando copper K-edge X-ray absorption spectroscopy (**d**) and high-resolution operando X-ray powder diffraction (XRD) (**e**, $\lambda = 0.1173$ Å) results of derived copper catalysts at 100 mA cm^{-2} in 1 M KOH at various CO concentrations. Ex situ copper K-edge X-ray absorption spectroscopy of copper foil is included in (**d**) as a reference.

These results surpass the best reported CORR $FE_{ethylene}$ (~40%) achieved at a potential of −0.72 V versus RHE (equivalent to a ~24% increase in cathodic energy efficiency)[9] by a factor of 1.6 in ethylene selectivity, and by a factor of 1.8 in cathodic energy efficiency. It represents the most efficient electrocatalytic CO to ethylene conversion reported so far (Supplementary Table 1). To assess further ethylene formation among only carbon-based products, we normalized ethylene selectivity by excluding the H_2 contribution. The normalized $FE_{ethylene}$ first increases and then reaches a plateau at a value of ~75% (Supplementary Fig. 30), which further supports the view that limiting CO availability on copper stabilizes intermediates favourable for ethylene.

To gain further insight into this ethylene formation strategy, we performed CORR in 1 M KOH at various CO concentrations and a fixed potential of −0.44 V versus RHE. With pure CO (100%), we observed a wide distribution of FEs for various products (Fig. 4e), in agreement with a recent CORR report[9]. Ethylene was the dominant product with an FE of ~30%. When we decreased the CO concentration from 100 to 5%, $FE_{ethylene}$ increased to ~50% at the expense of $FE_{1\text{-propanol}}$, and with little impact on $FE_{acetate}$, $FE_{ethanol}$ and FE_{H2}, confirming that an avenue to increase $FE_{ethylene}$ is to constrain CO. We noted a slight decrease of current densities at reduced CO concentrations, a feature we attributed to the lack of CO reactant and thus the sluggish CORR kinetics at these conditions (Supplementary Fig. 31).

With a further decrease of CO concentration from 5 to 2.5%, the lack of CO reactant manifests in substantial hydrogen production. This ethylene selectivity decrease highlights the fact that low CO availability promotes ethylene production only until to the mass transport limit. When the CO availability is decreased beyond

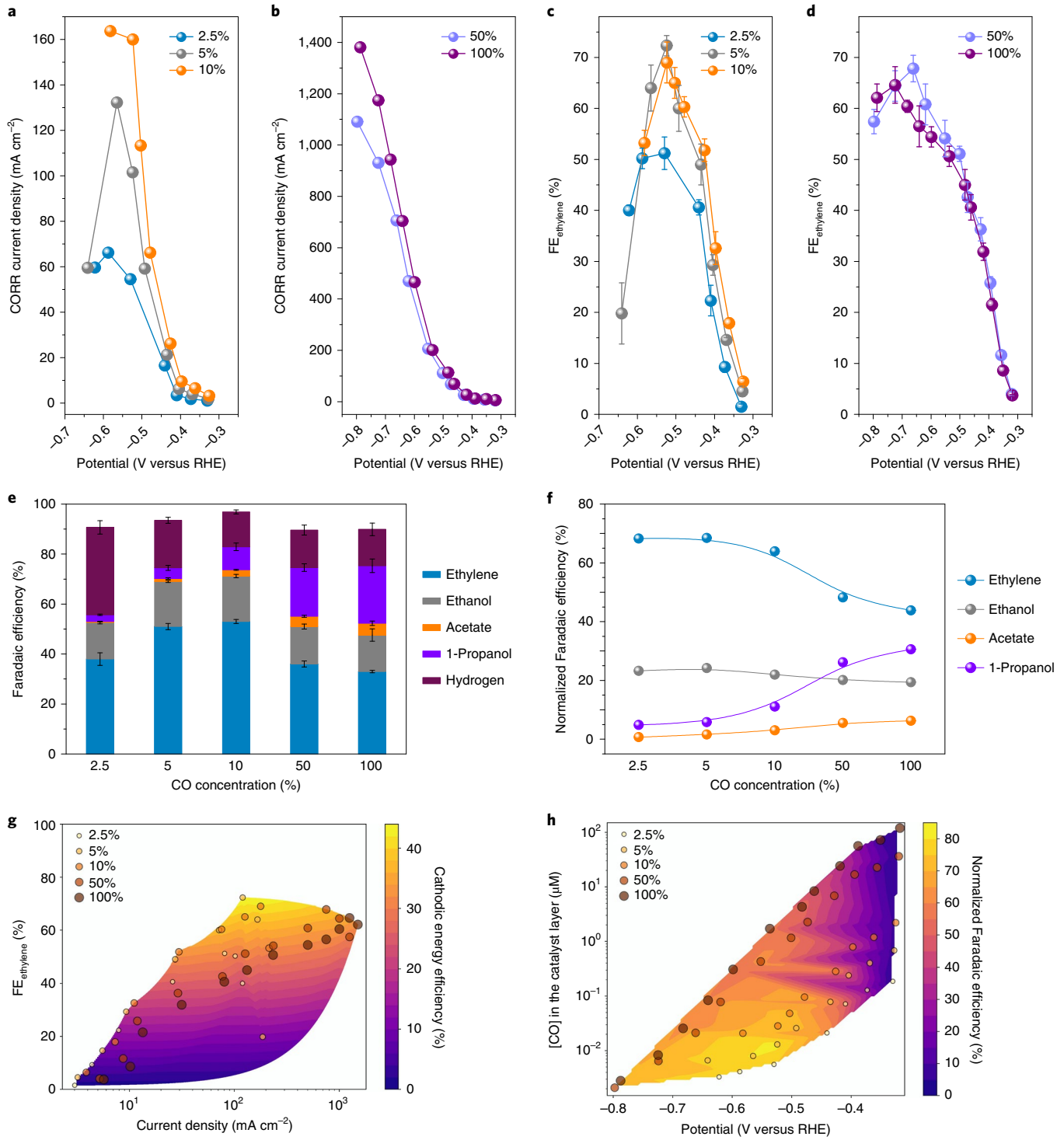

Fig. 4 | The performance of the CORR as a function of CO coverage. a–d, The CORR partial current densities (**a**,**b**) and $FE_{ethylene}$ (**c**,**d**) at low (**a**,**c**) and high (**b**,**d**) CO concentrations as a function of the applied potential in 1 M KOH. **e**,**f**, The FEs (**e**) and normalized FEs (**f**) of CORR products at different CO concentrations at an applied potential of −0.44 V versus RHE in 1 M KOH. **g**, A mapping of the cathodic energy efficiency and $FE_{ethylene}$ as a function of the current density. **h**, A mapping of normalized $FE_{ethylene}$ and the simulated local CO concentration in the catalyst layer as a function of applied potential. The error bars are means ± s.d. ($n = 3$ replicates). The heatmap in **g** was generated by linear interpolation using the griddata function of scipy (in Python 3.6) to interpolate between points and illustrate the broader relationships between the current density, $FE_{ethylene}$ and the cathodic energy efficiency. The heatmap values were interpolated from experimental values. Similarly, the heatmap in **h** was generated by linear interpolation to highlight the effect of the simulated local CO concentration and the applied potential on the normalized $FE_{ethylene}$.

the mass transport limit, either by increasing the reaction rate/potential at a fixed CO concentration (Fig. 4a–d) or lowering the input CO concentration at a fixed reaction rate/potential (Fig. 4e and Supplementary Fig. 32), ethylene selectivity reduces, in agreement with previous studies[19,35]. The key to ethylene production from CO is thus to constrain operating conditions such that CO

availability is neither too high (promoting oxygenates) nor too low (promoting hydrogen).

In all cases, the normalized $FE_{ethylene}$ (without hydrogen) shows a smooth trend of increased ethylene production with decreasing CO concentration (Fig. 4f). In terms of carbon products, we produce C_2 almost exclusively at low CO conditions (~70% of ethylene and ~25% of ethanol at a 2.5% CO) and we observe a product switching from ethylene to 1-propanol at higher CO concentrations. The development of operando/in situ techniques that are capable of tracking key C_{2+} intermediates[36] while operating at conditions relevant to flow cells would further our understanding of the C- and O- pathways branching in these systems.

The ethylene production performance—measured with FE, current density and cathodic energy efficiency—demonstrates a wide operating zone (Fig. 4g). By tuning conditions to constrain local CO availability, we achieve ethylene FEs (65–72%) and high cathodic energy efficiencies (35–44%), with current densities (120–1,250 mA cm^{-2}) well above the 100 mA cm^{-2} threshold. We further tested the system by reacting a simulated coke oven gas (Supplementary Fig. 33)—a by-product of industrial coke production in steel manufacturing—with a gaseous composition of 10% CO, 30% methane and 60% hydrogen[37,38]. We achieved stable CORR with this industrial mixture, producing $FE_{ethylene}$ of ~71% in 1 M KOH at a constant current density of 150 mA cm^{-2}.

For the conditions studied, we calculated the local CO concentration using a reaction–diffusion model and plot it against the potential and FE values that together determine the cathodic energy efficiency (Fig. 4h). The highest selectivities for ethylene correspond to low local CO concentrations, and are retained over a wide potential window from −0.5 to −0.8 V. The most energy-efficient combination of high selectivity and low overpotential occurs uniquely for low input CO stream concentrations.

Discussion

The findings of previous reports that assess the effect of CO partial pressure on ethylene electroproduction are varied. Schreier and co-workers[34] reported an unaltered ethylene partial current density with varying CO concentration from 100% to 10%, whereas Li and colleagues[19] showed decreasing ethylene partial current density at lower CO partial pressures. We discovered that these findings can be unified on the basis of CO availability. When we start from CO-rich conditions (that is, those not limited by CO mass transport), decreasing the CO partial pressure increases ethylene selectivity; however, a decrease in total current density (due to sluggish reaction kinetics at low CO concentrations) leads to little change in the ethylene partial current density (Supplementary Fig. 29), which is in agreement with the report by Schreier and colleagues[34]. By contrast, Li and co-workers[19] reduced the CO partial pressure from the initial condition of peak ethylene production from a 100% CO feed. Under these CO-deficient conditions, we also found that any decrease in the local CO concentration decreases ethylene selectivity, current density and ethylene partial current density (Supplementary Fig. 32).

The CO scarcity effect may play a role in ethylene production from CO_2 reduction[4,39,40]. Specifically, a wide potential gap of 200–300 mV for CO and ethylene formation has been observed from CO_2 reduction on copper catalysts[4,41,42] and the concentration of as-formed *CO intermediates on copper is low. In the CO_2RR, concentrated hydroxide ions accelerate the rate-determining step of the CO_2RR (that is, CO_2 to CO)[4], bridge the potential gap between CO and ethylene and also serve to limit the local CO availability as the high-pH electrolyte reduces the available CO_2 concentration. By contrast, the direct CORR achieves a higher local CO concentration on copper and risks diverting ethylene formation to other products. A high concentration of CO promotes CO dimerization and leads to a higher density of $*C_2$ intermediates at the catalysts–electrolyte interface. In a highly alkaline electrolyte these accumulated $*C_2$ species react with the abundant hydroxide ions to form acetate[9]. At more moderate pH values, the $*C_2$ can be further reduced to a C_3 product (that is, 1-propanol) that results from an intermolecular C–C coupling between $*C_2$ and adsorbed *CO species[17,18]. Constraining the local CO availability at catalyst surfaces in the CORR by tuning the incoming gas concentration and reaction rate provides the route to efficient ethylene production.

Carbon monoxide-induced surface restructuring of copper into nanoclusters has been shown to enhance the catalytic activity of copper[43–45]. To assess the potential role of copper nanoclusters in our system, we carried out CO partial pressure-dependent tests using commercial polycrystalline copper as electrocatalysts. By contrast to oxide-derived copper, polycrystalline copper does not produce nanoclusters during the CORR[38] nor does it exhibit product-specific sites for C_{2+} formations[21,45]. The measured ethylene selectivity of polycrystalline copper as a function of CO partial pressure (Supplementary Fig. 34) was similar to that of oxide-derived copper (Fig. 4e). We conclude that ethylene selectivity is dominated by CO availability and any surface restructuring in oxide-derived copper plays a lesser role.

In summary, tuning the local CO concentration at the catalyst surface enables efficient ethylene electrosynthesis. Constraining the local CO availability on the copper surface favours ethylene production, a trend seen in both simulations and experiments. We achieved a $FE_{ethylene}$ of ~70% over a wide range of CO concentrations and an ethylene partial current density of ~808 mA cm^{-2}. With this strategy, we combine low overpotential and high selectivity to achieve 44% half-cell ethylene energy efficiency. The performance here demonstrates efficient CO conversion to high-value C_2 chemicals that exceeds in terms of the critical metrics of output purity, energy efficiency and current density. Achieving these performance metrics with a dilute incoming stream presents further opportunities to convert dilute effluent streams directly into concentrated valued products.

Methods

DFT calculations. In this work, all of the DFT calculations were carried out with a periodic slab model using the Vienna ab initio simulation program[46–49]. The generalized gradient approximation was used with the Perdew–Burke–Ernzerhof[50] exchange-correlation functional. The projector-augmented wave method[51,52] was utilized to describe the electron–ion interactions, and the cut-off energy for the plane-wave basis set was 450 eV. To illustrate the long-range dispersion interactions between the adsorbates and catalysts, we employed the D3 correction method by Grimme et al.[53] Brillouin zone integration was accomplished using a 3×3×1 Monkhorst-Pack k-point mesh. Adsorption geometries were optimized using a force-based conjugate gradient algorithm, whereas transition states were located with a constrained minimization technique[54–56]. At the intermediate and transition states, one charged layer of water molecules was added to the surface to take the combined field and solvation effects into account[26]. The crystal structure was optimized for the modelling of Cu(100), which was modelled with a periodic four-layer p(3×3) model with the two lower layers fixed and two upper layers relaxed. The atomic coordinates of the optimized models—including the structures of initial states and transition states—are provided in Supplementary Data 1.

Preparation of electrocatalysts and a gas diffusion electrode. All reagents used in this work were from Sigma Aldrich without further purification. The copper oxide precatalysts were synthesized using a method reported earlier[57]. First, 4.5 g of triblock copolymer Pluronic P123 (MW 5800) was dispersed in 200 ml deionized water under a continuous stirring to form a clear solution. A 20 ml dark blue solution comprising 0.4 g copper(II) fluoride ($CuF_2{\cdot}2H_2O$), 3 ml ammonia (~30%) and deionized water was added and well stirred. Finally, 0.6 M of L-ascorbic acid solution was made and added drop by drop into the above solution using a syringe until an orange suspension was formed, indicating the formation of copper oxide nanoparticles. The as-made product was rinsed with ethanol, centrifuged three times and dried overnight under vacuum at room temperature (~20 °C). The preparation of a gas diffusion electrode was made by airbrushing (using N_2 as a carrier gas) a precatalyst ink comprising 30 mg of as-made oxide precatalysts, 3 ml isopropanol and 120 µl Nafion solution (~5 wt%) onto a commercial Sigracet gas diffusion layer (Fuel Cell store) with a size of 4×6 cm^2. The areal loading amount is ~1 mg cm^{-2}. After vacuum drying, a 2×2 cm^2 gas diffusion electrode was cut

and assembled into a flow cell electrolyser (Supplementary Fig. 1). Active copper electrocatalysts were then derived under the operando CORR condition.

Characterization. The surface morphology was analysed using a Hitachi SU9000 SEM/STEM at 2 kV. Operando hard X-ray absorption spectroscopy measurements were conducted at beamline 9BM of the Advanced Photon Source (APS). High-resolution operando XRD tests were performed at the beamline 11-ID-C ($\lambda = 0.1173$ Å) of APS using a homemade flow cell (Supplementary Fig. 26). Operando measurements were performed at 100 mA cm^{-2} in 1 M KOH.

Electrochemical reduction of CO. All CO reduction experiments were performed using a three-electrode flow cell electrolyser (see detailed sketches of the flow reactor design in Supplementary Fig. 1)[4,58]. The as-made gas diffusion electrode, Ag/AgCl (filled with 1 M KCl) and nickel foam (1.6 mm thickness, MTI Corporation) were used as cathode, reference electrode and anode, respectively. Alkaline solutions with various KOH concentrations were used as electrolytes at both cathode and anode sides. An anion exchange membrane (Fumasep FAA-PK-130) was sandwiched between catholyte and anolyte compartments to avoid product crossover. An Autolab PGSTAT204 (Metrohm Autolab) in combination with a BOOSTER10A module (Metrohm Autolab) was used as a power supply. During the CORR experiment, an aqueous KOH solution was individually directed into and circulated through the cathode and anode compartments with the assistance of two variable-speed peristaltic tubing pumps (Control Company 3385). A continuously flowing 60 s.c.c.m. CO gas or CO/N_2 mixed gas was directed into the gas compartment and reacted at the catalyst–catholyte interface by gas diffusion through the gas diffusion layer.

Applied cathode potentials after iR_{cell} compensation (i is the applied current and R_{cell} is the cell resistance) were converted to the RHE reference scale using $E_{RHE} = E_{Ag/AgC} + 0.235\,V + 0.059 \times pH$; iR_{cell} compensation was performed using the equation:

$$E_{cat} = E_{applied} - 0.85 \times I_{total} \times R_{cell} \quad (2)$$

where E_{cat} is the iR_{cell}-corrected potential at the cathode, $E_{applied}$ is the applied potential before iR_{cell} correction, I_{total} is the total current (a negative value at the cathode), and R_{cell} is determined to be 3.31 Ω by performing an electrochemical impedance spectroscopy measurement using an Autolab PGSTAT302N electrochemical workstation coupled with a FRA32M module. A factor of 0.85 is applied in iR_{cell} compensation during flow cell operation due to a low resistivity of 1 M KOH electrolyte, which holds a relatively low voltage drop over the electrolyte.

Gas and liquid products were respectively analysed using a gas chromatograph (PerkinElmer Clarus 680) and a one-dimensional ^{1}H NMR coupled with a Agilent DD2 500 spectrometer[4], in which diluted dimethyl sulfoxide in D_2O was used as an internal standard for the identification and quantification of liquid products.

$FE_{ethylene}$ was calculated using the equation[9]:

$$FE(\%) = \frac{nFxV}{j_{total}} \times 100 \quad (3)$$

where n is the number of electrons transferred, F is Faraday's constant, x is the mole fraction of ethylene, V is the total molar flow rate of gas reactant and j_{total} is the total current applied during the CORR.

COMSOL modelling. The CO and OH^- concentrations were modelled in COMSOL (COMSOL Multiphysics) using a 1D reaction–diffusion model as outlined in Supplementary Note 3.

Data availability

The data that support the findings of this study are available from the corresponding author on reasonable request.

Received: 22 January 2019; Accepted: 7 October 2019;
Published online: 11 November 2019

References

1. Seh, Z. W. et al. Combining theory and experiment in electrocatalysis: insights into materials design. *Science* **355**, eaad4998 (2017).
2. Zhang, L., Zhao, Z. J. & Gong, J. L. Nanostructured materials for heterogeneous electrocatalytic CO_2 reduction and their related reaction mechanisms. *Angew. Chem. Int. Ed.* **56**, 11326–11353 (2017).
3. Zheng, X. L. et al. Theory-guided Sn/Cu alloying for efficient CO_2 electroreduction at low overpotentials. *Nat. Catal.* **2**, 55–61 (2019).
4. Dinh, C. T. et al. CO_2 electroreduction to ethylene via hydroxide-mediated copper catalysis at an abrupt interface. *Science* **360**, 783–787 (2018).
5. De Luna, P. et al. Catalyst electro-redeposition controls morphology and oxidation state for selective carbon dioxide reduction. *Nat. Catal.* **1**, 103–110 (2018).
6. Zhuang, T. T. et al. Steering post-C–C coupling selectivity enables high efficiency electroreduction of carbon dioxide to multi-carbon alcohols. *Nat. Catal.* **1**, 421–428 (2018).
7. Zhou, Y. S. et al. Dopant-induced electron localization drives CO_2 reduction to C_2 hydrocarbons. *Nat. Chem.* **10**, 974–980 (2018).
8. Li, C. W., Ciston, J. & Kanan, M. W. Electroreduction of carbon monoxide to liquid fuel on oxide-derived nanocrystalline copper. *Nature* **508**, 504–507 (2014).
9. Jouny, M., Luc, W. & Jiao, F. High-rate electroreduction of carbon monoxide to multi-carbon products. *Nat. Catal.* **1**, 748–755 (2018).
10. Liu, M. et al. Enhanced electrocatalytic CO_2 reduction via field-induced reagent concentration. *Nature* **537**, 382–386 (2016).
11. Haas, T., Krause, R., Weber, R., Demler, M. & Schmid, G. Technical photosynthesis involving CO_2 electrolysis and fermentation. *Nat. Catal.* **1**, 32–39 (2018).
12. Schreier, M. et al. Solar conversion of CO_2 to CO using earth-abundant electrocatalysts prepared by atomic layer modification of CuO. *Nat. Energy* **2**, 17087 (2017).
13. Li, J. et al. Efficient electrocatalytic CO_2 reduction on a three-phase interface. *Nat. Catal.* **1**, 592–600 (2018).
14. Spurgeon, J. M. & Kumar, B. A comparative technoeconomic analysis of pathways for commercial electrochemical CO_2 reduction to liquid products. *Energy Environ. Sci.* **11**, 1536–1551 (2018).
15. Jouny, M., Luc, W. & Jiao, F. General techno-economic analysis of CO_2 electrolysis systems. *Ind. Eng. Chem. Res.* **57**, 2165–2177 (2018).
16. Han, L. H., Zhou, W. & Xiang, C. X. High-rate electrochemical reduction of carbon monoxide to ethylene using Cu-nanoparticle-based gas diffusion electrodes. *ACS Energy Lett.* **3**, 855–860 (2018).
17. Zhuang, T. T. et al. Copper nanocavities confine intermediates for efficient electrosynthesis of C_3 alcohol fuels from carbon monoxide. *Nat. Catal.* **1**, 946–951 (2018).
18. Pang, Y. J. et al. Efficient electrocatalytic conversion of carbon monoxide to propanol using fragmented copper. *Nat. Catal.* **2**, 251–258 (2019).
19. Li, J. et al. Effectively increased efficiency for electroreduction of carbon monoxide using supported polycrystalline copper powder electrocatalysts. *ACS Catal.* **9**, 4709–4718 (2019).
20. Gabardo, C. M. et al. Combined high alkalinity and pressurization enable efficient CO_2 electroreduction to CO. *Energy Environ. Sci.* **11**, 2531–2539 (2018).
21. Lum, Y. W. & Ager, J. W. Evidence for product-specific active sites on oxide-derived Cu catalysts for electrochemical CO_2 reduction. *Nat. Catal.* **2**, 86–93 (2019).
22. Xiao, H., Cheng, T. & Goddard, W. A. Atomistic mechanisms underlying selectivities in C_1 and C_2 products from electrochemical reduction of CO on Cu(111). *J. Am. Chem. Soc.* **139**, 130–136 (2017).
23. Lum, Y. W., Cheng, T., Goddard, W. A. & Ager, J. W. Electrochemical CO reduction builds solvent water into oxygenate products. *J. Am. Chem. Soc.* **140**, 9337–9340 (2018).
24. Cheng, T., Xiao, H. & Goddard, W. A. Full atomistic reaction mechanism with kinetics for CO reduction on Cu(100) from ab initio molecular dynamics free-energy calculations at 298 K. *Proc. Natl Acad. Sci. USA* **114**, 1795–1800 (2017).
25. Lausche, A. C. et al. On the effect of coverage-dependent adsorbate-adsorbate interactions for CO methanation on transition metal surfaces. *J. Catal.* **307**, 275–282 (2013).
26. Montoya, J. H., Shi, C., Chan, K. & Nørskov, J. K. Theoretical insights into a CO dimerization mechanism in CO_2 electroreduction. *J. Phys. Chem. Lett.* **6**, 2032–2037 (2015).
27. Liu, X. Y. et al. Understanding trends in electrochemical carbon dioxide reduction rates. *Nat. Commun.* **8**, 15438 (2017).
28. Sandberg, R. B., Montoya, J. H., Chan, K. & Nørskov, J. K. CO–CO coupling on Cu facets: coverage, strain and field effects. *Surf. Sci.* **654**, 56–62 (2016).
29. Nørskov, J. K. et al. Origin of the overpotential for oxygen reduction at a fuel-cell cathode. *J. Phys. Chem. B* **108**, 17886–17892 (2004).
30. Schouten, K. J. P., Qin, Z., Pérez Gallent, E. & Koper, M. T. Two pathways for the formation of ethylene in CO reduction on single-crystal copper electrodes. *J. Am. Chem. Soc.* **134**, 9864–9867 (2012).
31. Wang, Z., Cao, X. M., Zhu, J. & Hu, P. Activity and coke formation of nickel and nickel carbide in dry reforming: a deactivation scheme from density functional theory. *J. Catal.* **311**, 469–480 (2014).
32. Wang, Z., Wang, H.-F. & Hu, P. Possibility of designing catalysts beyond the traditional volcano curve: a theoretical framework for multi-phase surfaces. *Chem. Sci.* **6**, 5703–5711 (2015).
33. Liu, Q. et al. Approaching the capacity limit of lithium cobalt oxide in lithium ion batteries via lanthanum and aluminium doping. *Nat. Energy* **3**, 936–943 (2018).
34. Schreier, M., Yoon, Y., Jackson, M. N. & Surendranath, Y. Competition between H and CO for active sites governs copper-mediated electrosynthesis of hydrocarbon fuels. *Angew. Chem., Int. Ed.* **57**, 10221–10225 (2018).
35. Wang, L. et al. Electrochemical carbon monoxide reduction on polycrystalline copper: effects of potential, pressure, and pH on selectivity toward multicarbon and oxygenated products. *ACS Catal.* **8**, 7445–7454 (2018).
36. Handoko, A. D., Wei, F., Yeo, B. S. & Seh, Z. W. Understanding heterogeneous electrocatalytic carbon dioxide reduction through operando techniques. *Nat. Catal.* **1**, 922–934 (2018).

37. Razzaq, R., Li, C. & Zhang, S. Coke oven gas: availability, properties, purification, and utilization in China. *Fuel* **113**, 287–299 (2013).
38. Wang, S., Wang, G., Jiang, F., Luo, M. & Li, H. Chemical looping combustion of coke oven gas by using Fe_2O_3/CuO with $MgAl_2O_4$ as oxygen carrier. *Energy Environ. Sci.* **3**, 1353–1360 (2010).
39. Hoang, T. T. H., Ma, S. C., Gold, J. I., Kenis, P. J. A. & Gewirth, A. A. Nanoporous copper films by additive-controlled electrodeposition: CO_2 reduction catalysis. *ACS Catal.* **7**, 3313–3321 (2017).
40. Hoang, T. T. H. et al. Nanoporous copper silver alloys by additive-controlled electrodeposition for the selective electroreduction of CO_2 to ethylene and ethanol. *J. Am. Chem. Soc.* **140**, 5791–5797 (2018).
41. Ma, S. C. et al. One-step electrosynthesis of ethylene and ethanol from CO_2 in an alkaline electrolyzer. *J. Power Sources* **301**, 219–228 (2016).
42. Huang, Y., Handoko, A. D., Hirunsit, P. & Yeo, B. S. Electrochemical reduction of CO_2 using copper single-crystal surfaces: effects of CO* coverage on the selective formation of ethylene. *ACS Catal.* **7**, 1749–1756 (2017).
43. Eren, B. et al. Activation of Cu(111) surface by decomposition into nanoclusters driven by CO adsorption. *Science* **351**, 475–478 (2016).
44. Eren, B. et al. One-dimensional nanoclustering of the Cu(100) surface under CO gas in the mbar pressure range. *Surf. Sci.* **651**, 210–214 (2016).
45. Li, J. et al. Copper adparticle enabled selective electrosynthesis of n-propanol. *Nat. Commun.* **9**, 4614 (2018).
46. Kresse, G. & Furthmuller, J. Efficient iterative schemes for ab initio total-energy calculations using a plane-wave basis set. *Phys. Rev. B* **54**, 11169–11186 (1996).
47. Kresse, G. & Furthmuller, J. Efficiency of ab-initio total energy calculations for metals and semiconductors using a plane-wave basis set. *Comput. Mater. Sci.* **6**, 15–50 (1996).
48. Kresse, G. & Hafner, J. Ab-initio molecular-dynamics simulation of the liquid-metal amorphous–semiconductor transition in germanium. *Phys. Rev. B* **49**, 14251–14269 (1994).
49. Kresse, G. & Hafner, J. Ab initio molecular dynamics for liquid metals. *Phys. Rev. B* **47**, 558–561 (1993).
50. Perdew, J. P., Burke, K. & Ernzerhof, M. Generalized gradient approximation made simple. *Phys. Rev. Lett.* **77**, 3865–3868 (1996).
51. Kresse, G. & Joubert, D. From ultrasoft pseudopotentials to the projector augmented-wave method. *Phys. Rev. B* **59**, 1758–1775 (1999).
52. Blochl, P. E. Projector augmented-wave method. *Phys. Rev. B* **50**, 17953–17979 (1994).
53. Grimme, S., Antony, J., Ehrlich, S. & Krieg, H. A consistent and accurate ab initio parametrization of density functional dispersion correction (DFT-D) for the 94 elements H–Pu. *J. Chem. Phys.* **132**, 154104 (2010).
54. Alavi, A., Hu, P., Deutsch, T., Silvestrelli, P. L. & Hutter, J. CO oxidation on Pt(111): an *ab initio* density functional theory study. *Phys. Rev. Lett.* **80**, 3650 (1998).
55. Michaelides, A. et al. Identification of general linear relationships between activation energies and enthalpy changes for dissociation reactions at surfaces. *J. Am. Chem. Soc.* **125**, 3704–3705 (2003).
56. Liu, Z. P. & Hu, P. General rules for predicting where a catalytic reaction should occur on metal surfaces: a density functional theory study of C–H and C–O bond breaking/making on flat, stepped, and kinked metal surfaces. *J. Am. Chem. Soc.* **125**, 1958–1967 (2003).
57. Shang, Y., Zhang, D. F. & Guo, L. CuCl-intermediated construction of short-range-ordered Cu_2O mesoporous spheres with excellent adsorption performance. *J. Mater. Chem.* **22**, 856–861 (2012).
58. Jhong, H. R. M., Brushett, F. R. & Kenis, P. J. The effects of catalyst layer deposition methodology on electrode performance. *Adv. Energy Mater.* **3**, 589–599 (2013).

Acknowledgements

This work was supported financially by the Ontario Research Fund: Research Excellence programme, the Natural Sciences and Engineering Research Council of Canada, the CIFAR Bio-inspired Solar Energy programme and the University of Toronto Connaught grant. This research used synchrotron resources of the APS, an Office of Science user facility that is operated for the US Department of Energy Office of Science by Argonne National Laboratory and was supported by the US Department of Energy under contract no. DE-AC02-06CH11357, as well as the Canadian Light Source and its funding partners. This research also used infrastructure provided by the Canada Foundation for Innovation and the Ontario Research Fund. The authors thank T.P. Wu, Y.Z. Finfrock and L. Ma for technical support at the 9BM beamline of APS. D.S. acknowledges the Natural Sciences and Engineering Research Council E.W.R Steacie Memorial Fellowship. J.L. acknowledges the Banting Postdoctoral Fellowships programme. C.M.G. acknowledges the Natural Sciences and Engineering Research Council Postdoctoral Fellowships programme. All of the DFT computations were performed on the IBM BlueGene/Q supercomputer with support from the Southern Ontario Smart Computing Innovation Platform and Niagara supercomputer at the SciNet HPC Consortium. The Southern Ontario Smart Computing Innovation Platform is funded by the Federal Economic Development Agency of Southern Ontario, the Province of Ontario, IBM Canada Ltd., Ontario Centres of Excellence, Mitacs and 15 Ontario academic member institutions. SciNet is funded by: the Canada Foundation for Innovation; the Government of Ontario; Ontario Research Fund - Research Excellence; and the University of Toronto.

Author contributions

E.H.S and D.S. supervised the project. J.L. designed and carried out all the experiments. Z.Y.W. performed the DFT simulation. C.M. simulated the diffusion-reaction. J.Y.H. conducted the SEM characterization. F.W.L., L.W., and Y.R. assisted the operando XRD measurements and data analysis. Y.X., Y.H.W., C.M.G., C.T.D. and T.T.Z. contributed in data analysis and manuscript polishing. All authors discussed the results and assisted during manuscript preparation.

Competing interests

The authors declare no competing interests.

Additional information

Supplementary information is available for this paper at https://doi.org/10.1038/s41929-019-0380-x.

Correspondence and requests for materials should be addressed to E.H.S. or D.S.

Reprints and permissions information is available at www.nature.com/reprints.

Publisher's note Springer Nature remains neutral with regard to jurisdictional claims in published maps and institutional affiliations.